

# INVESTIGATING THE INFLUENCE OF AN INBOARD PROPELLER'S VERTICAL OFFSET ON A TRAILING WING'S LIFT AND DRAG DISTRIBUTIONS

Shamsheer S. Chauhan<sup>1</sup>, Gustavo Padovany da Silva<sup>2</sup>, Gustavo L. O. Halila<sup>3</sup>, Joaquim R. R. A. Martins<sup>1</sup> & João Luiz F. Azevedo<sup>4</sup>

<sup>1</sup>University of Michigan, Ann Arbor, MI, USA.
<sup>2</sup>Universidade Federal do Paraná, 81530-900 Curitiba, PR, Brazil.
<sup>3</sup>Embraer, 12227-901 São José dos Campos, SP, Brazil.
<sup>4</sup>Instituto de Aeronáutica e Espaço, 12228-904 São José dos Campos, SP, Brazil.

## **Abstract**

Propeller-wing interaction has been a topic of investigation since the dawn of aviation. Surprisingly, however, there are few published studies showing how changing a tractor propeller's vertical offset affects a trailing wing's lift and drag distributions. In this work, we investigate this for a rectangular wing with an inboard propeller using steady Reynolds-averaged Navier—Stokes computational fluid dynamics and an actuator-disk approach. We present results for two angles of attack and a range of propeller-wing vertical offsets for both inboard-up and outboard-up propeller rotation. We include plots for spanwise sectional lift and drag coefficient distributions, integrated lift and drag coefficients, lift-to-drag ratios, and chordwise sectional pressure-coefficient distributions. The results show that changing the propeller-wing vertical offset can significantly change a trailing wing's lift and drag distributions, which strongly depend on the direction of the vertical offset.

**Keywords:** CFD, propeller-wing interference, propeller vertical location

# Nomenclature

 $\mu$  = Dynamic viscosity

v = Rotation rate

 $\rho$  = Density

b = Wing span

 $C_D$  = Integrated drag coefficient of the wing

 $C_d$  = Sectional drag coefficient

 $C_L$  = Integrated lift coefficient of the wing

 $C_l$  = Sectional lift coefficient

 $C_p$  = Pressure coefficient

D = Drag

 $D_{\emptyset}$  = Propeller diameter

*F* = Propeller-model force parameter

 $f_x$  = Axial force per unit radius

 $f_{\theta}$  = Tangential force per unit radius

J = Propeller advance ratio,  $V_{\infty}/(vD_{\varnothing})$ 

L = Lift

*n* = Propeller-model shape parameter

P = Propeller pitch
R = Propeller radius
r = Radial coordinate

 $\hat{r}$  = Normalized radius,  $(r - r_{in})/(R - r_{in})$ 

 $r_{in}$  = Inner radius

T = Thrust

 $T_C$  = Thrust coefficient,  $T/(\rho V_{\infty}^2 D_{\varnothing}^2)$ 

 $V_{\infty}$  = Freestream velocity

## 1. Introduction

Propeller-wing interaction has been a topic of interest and investigation since the early days of aviation [1–4]. Recently, the interest in developing electric vertical or short takeoff and landing (eV/STOL) aircraft has led to a resurgence of interest in understanding and accurately capturing propeller-wing interaction effects using computational tools [5–16].

When a propeller is located near a wing, the flow induced by the propeller affects both the lift and the drag of the wing. The nature of the influence depends on the propeller's location and rotation direction [1,17–21]. When located directly in front of the wing, the propeller's axial and tangential induced-velocity components create spanwise variations in the wing's local angles of attack and effective freestream speeds. Additionally, when a propeller is vertically offset relative to a wing, the pressure and velocity distributions associated with streamtube contraction also affect the lift and drag of the wing, even when the slipstream does not impinge directly on the wing [1,20]. This paper investigates the effect of propeller-wing vertical offset on a trailing wing's lift and drag distributions. There is a lack of literature showing computational or experimental results for this.

Prandtl [1] and Veldhuis [20] investigated the effect of propeller-wing vertical offset on a trailing wing's lift and drag using experimental methods. They presented integrated lift and drag coefficient ( $C_L$  and  $C_D$ ) results for a range of positive and negative vertical offsets, and they attributed the non-monotonic trends to two primary factors. The first factor is a combination of the non-uniform radial distribution of dynamic pressure in a propeller's streamtube and the varying extent of the wing inside the propeller's streamtube. The second factor is the pressure and velocity distributions associated with streamtube contraction. The second factor is responsible for their observations that when the propeller is located close to the wing but not close enough for the wing to be inside the streamtube, the lift is greater for a positive vertical offset (above the wing) than for a negative vertical offset. Their results are limited to integrated lift and drag coefficients and do not include results showing the effect of propeller-wing vertical offset on spanwise lift and drag distributions.

There are many approaches of varying complexity and fidelity that can be used to model propeller-wing interaction [7, 8, 10, 11, 13–16, 18–20, 22–38]. These include vortex-lattice approaches [20, 23, 24, 31–34] and computational fluid dynamics (CFD) approaches [7, 11, 13, 14, 16, 20, 22, 26–29, 35–39]. The vortex-lattice approaches have limitations related to viscous effects, thickness effects, and streamtube modification. The CFD approaches can capture those effects more directly but have significantly higher computational costs.

The approach of using steady CFD with an actuator disk has been shown to provide accurate time-averaged predictions for a wing located behind a propeller [16,20,26,29,35]. This approach provides a tractable balance of fidelity and cost that is suitable for design studies requiring large numbers of simulations. Therefore, we use an actuator-disk CFD approach for this work.

In this paper, we present CFD results for a rectangular wing with an inboard tractor propeller using steady Reynolds-averaged Navier–Stokes (RANS) CFD and an actuator-disk approach. We present results for two angles of attack and a range of propeller-wing vertical offsets for both inboard-up and outboard-up propeller rotation. We include plots for spanwise sectional lift and drag coefficient distributions, integrated lift and drag coefficients, lift-to-drag ratios, and chordwise sectional pressure-

coefficient distributions.

# 2. Computational Tools

For this work, we use open-source modules of the MDO of Aircraft Configurations with High Fidelity (MACH) framework [40] <sup>1</sup>.

## 2.1 Flow Solver

For this study, we use the open-source CFD solver ADflow [41,42] modified to implement an actuator-disk propeller model [11,16]. ADflow is a second-order-accurate finite-volume CFD solver that solves the flow equations on structured multiblock meshes, and it supports overset meshes using implicit hole cutting [43–45]. ADflow has options to solve the Euler, laminar Navier–Stokes, and RANS equations. For this work, we solve the steady RANS equations with the Spalart–Allmaras (SA) turbulence model [46]. The SA implementation used here is the SA-noft2 variant described in the NASA Turbulence Modeling Resource <sup>2</sup>, and the production term is computed using strain.

We use the Jameson–Schmidt–Turkel scheme with scalar dissipation [47] for inviscid fluxes, and the viscous flux gradients are calculated using the Green–Gauss approach. A pseudo-transient continuation (PTC) strategy is used to converge the flow equations, and multiple algorithms are available. For this work, we use the approximate Newton–Krylov (ANK) solver [41] and converge the total residual norm by eight orders of magnitude.

The simulations for this work were performed on a laptop with an Intel i9-12900H processor and 32 GB of RAM, and the mean wall time per simulation is 20 minutes using ten processors.

## 2.2 Mesh Generation

For this study, we use MACH's pySpline<sup>3</sup> and pyGeo<sup>4</sup> modules to generate the wing surface geometry. We generate the wing surface mesh and the propeller-region volume mesh using the commercial package ICEM-CFD.

To generate the wing volume mesh and the background volume mesh, we use MACH's pyHyp<sup>5</sup> [48] module. The pyHyp module uses a hyperbolic mesh marching method [49] to produce high-quality volume meshes by extruding structured surface meshes. The primary user-defined parameters are the height of the first layer of cells, the extrusion distance, and the number of layers. These volume meshes are structured multiblock meshes, and we combine them using the open-source tool cgnsUtilities<sup>6</sup> to obtain an overset mesh. We also use cgnsUtilities to change the location of the propeller-region volume mesh for the different propeller locations studied in this work. This overset approach allows for the effortless generation of new meshes for these propeller locations.

## 2.3 Propeller Model

We model the propeller using an actuator-disk approach in which terms corresponding to propeller forces are added to the momentum and energy equations in the manner of body forces [16, 22]. We use the following model [50] for the distributions of the axial and tangential loading. The radial distribution of the axial force is given by

$$f_x = F\hat{r}(1-\hat{r})^n, \tag{1}$$

<sup>1</sup>www.github.com/mdolab/MACH-Aero

 $<sup>^2</sup>$ https://turbmodels.larc.nasa.gov/spalart.html

<sup>3</sup>https://github.com/mdolab/pyspline

<sup>4</sup>https://github.com/mdolab/pygeo

<sup>5</sup>https://github.com/mdolab/pyhyp

<sup>6</sup>https://github.com/mdolab/cgnsutilities

where  $f_x$  is the axial force per unit radius,  $\hat{r}$  is defined by Eq. (2), n is a parameter that controls the shape of the distribution, and F is a value computed by integrating this expression over the radius and equating it to the total thrust T. The normalized radius  $\hat{r}$  is defined as

$$\hat{r} = \frac{r - r_{\text{in}}}{R - r_{\text{in}}},\tag{2}$$

where r is the radial distance from the axis of rotation,  $r_{in}$  is the inner radius of the propeller, and R is the outer radius of the propeller. The radial distribution of the tangential force is given by

$$f_{\theta} = f_x \left( \frac{P/D_{\varnothing}}{\pi(r/R)} \right), \tag{3}$$

where  $f_{\theta}$  is the tangential force per unit radius, and  $P/D_{\emptyset}$  is the propeller pitch-to-diameter ratio.

# 3. Problem Description

# 3.1 Geometry and Specifications

The baseline configuration, shown in Fig. 1, is a rectangular wing with a tractor propeller located at  $47\% \ b/2$ , where b/2 is the half-span. The wing is not swept, twisted, or tapered, and the propeller axis is aligned with the wing section's chord line and has no vertical offset relative to it. The wing airfoil is NACA  $64_2$ -A015, and we use coordinates from the online UIUC database [51]. We do not model the nacelle, nor do we round the leading edge of the wingtip.

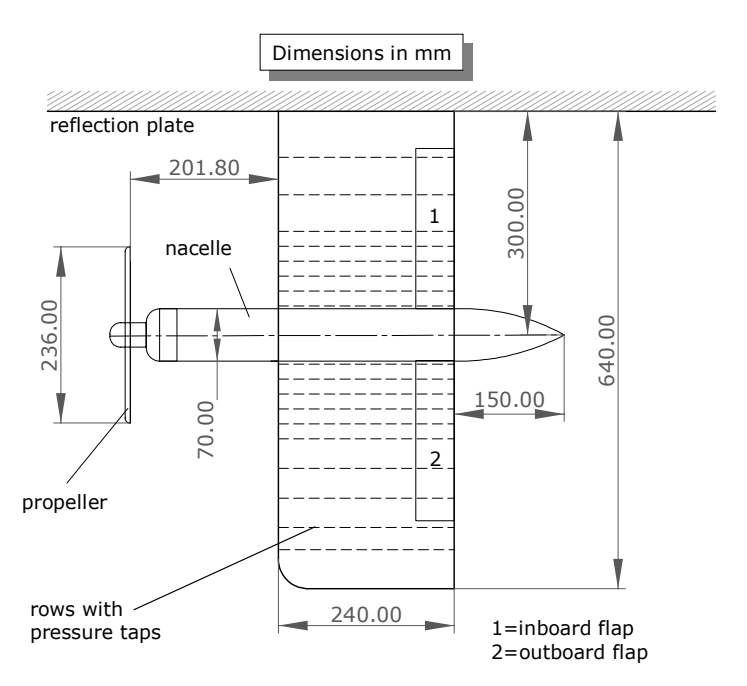


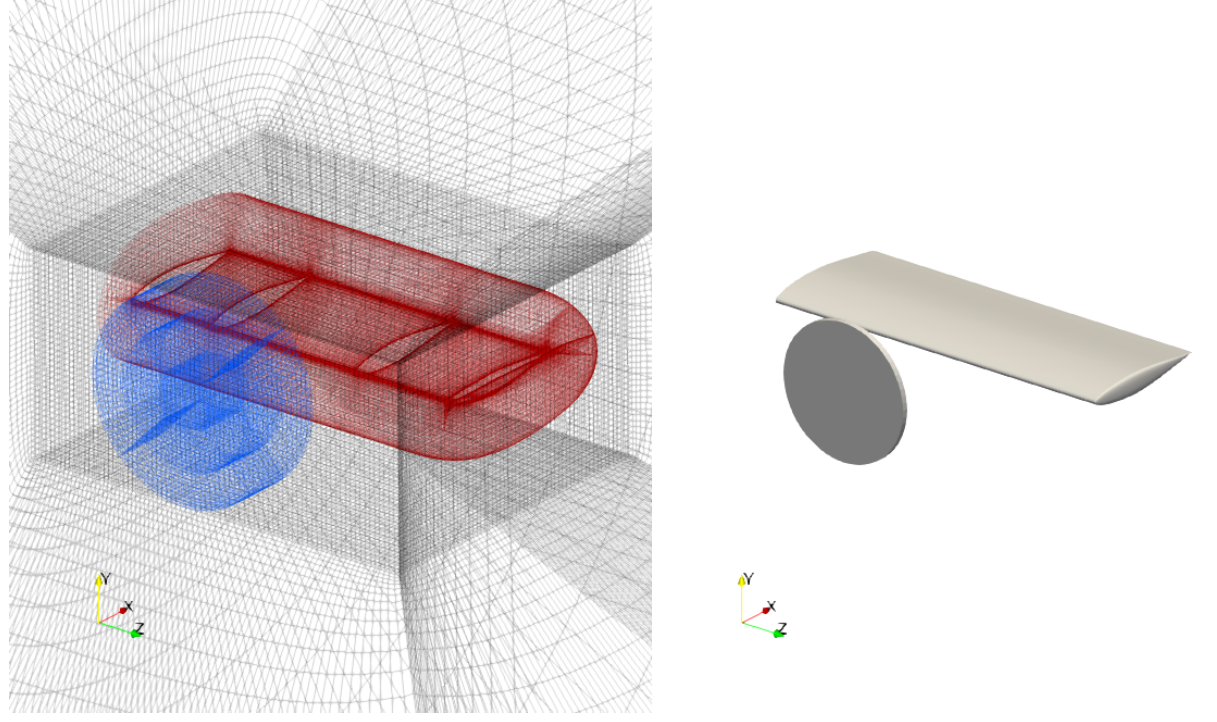
Figure 1 – Original geometry of the baseline configuration (half-wing planform area is 0.15 m<sup>2</sup>; aspect ratio is 5.3; reproduced with permission from Veldhuis [20])

The Reynolds number and freestream dynamic pressure reported for the experimental cases are  $0.8 \cdot 10^6$  and  $1500 \, \text{Pa}$ , respectively [20]. For the fluid properties, we use standard sea-level values. The propeller operates at an advance ratio of  $J = V_{\infty}/(vD_{\varnothing}) = 0.85$  and a thrust coefficient of  $T_C = T/(\rho V_{\infty}^2 D_{\varnothing}^2) = 0.168$  [20]. Here,  $V_{\infty}$  is the freestream velocity, v is the rotation rate,  $D_{\varnothing}$  is the propeller diameter,  $\rho$  is the freestream density, and T is the propeller thrust.

We previously presented validation and mesh refinement results in an earlier paper [16] using this configuration and the same baseline meshes and propeller model used here. For the validation study, we compared our results with experimental results for 0 and 4 deg angle-of-attack (AoA) cases [16]. For this work, we use the same two angles of attack. We change the angle of attack in these simulations by changing the direction of the freestream velocity. This maintains the relative orientations of the actuator disk and the wing.

#### 3.2 CFD Volume Meshes

Each case's mesh consists of a wing volume mesh, a cylindrical volume mesh for the propeller region, and a background volume mesh. The outlines of the blocks of these meshes are shown in Fig. 2a for the baseline configuration. Force terms are applied to the cells in the cylindrical volume mesh that lie inside a user-specified disk surface (visualized in Fig. 2b for the baseline configuration). The wing surface mesh is generated using the commercial package ICEM-CFD. The wing volume mesh is generated by extruding the wing surface mesh using MACH's pyHyp [48] module.



- (a) Wing and propeller-region volume meshes overset with a background volume mesh
- (b) Disk surface used to specify the actuator zone

Figure 2 – Baseline configuration surfaces and volume meshes

Each background mesh consists of a Cartesian volume mesh encapsulating the wing and propeller-region meshes. The outer surfaces of these Cartesian meshes are extruded by 45 chord lengths, resulting in hemispherical domains. We use far-field boundary conditions for the outer hemispherical surface of the domain and symmetry boundary conditions for the plane coincident with the root of the wing. The propeller-region volume mesh is larger than the disk of cells to which the actuator forces are applied, in order to allow it to be overset with the background mesh. ADflow uses an implicit hole-cutting method for connecting the overset meshes [43–45].

To change the vertical offset of the propeller for this study, we reposition the propeller-region volume mesh and regenerate the background mesh as shown in Fig. 3. Figure 4 shows the corresponding disk surfaces for specifying the actuator zone. The midplanes of the cells that are selected for the actuator zones are located 0.2 m in front of the wing. The radius of the actuator zone is the propeller radius of 0.12 m, and its thickness is 9 mm (one layer of cells).

We generate the wing volume mesh by extruding the wing surface mesh by 0.4 chord lengths using pyHyp. The wing volume mesh has 40 layers of cells, and the maximum growth ratios of these layers in the off-wall directions range from 1.2 to 1.3. The cell thickness of the first off-wall layer is set to a flat-plate y+ value of 1.

We previously presented validation and mesh refinement results using this configuration in an earlier paper [16], and this work re-uses the Level-2 meshes from that work.

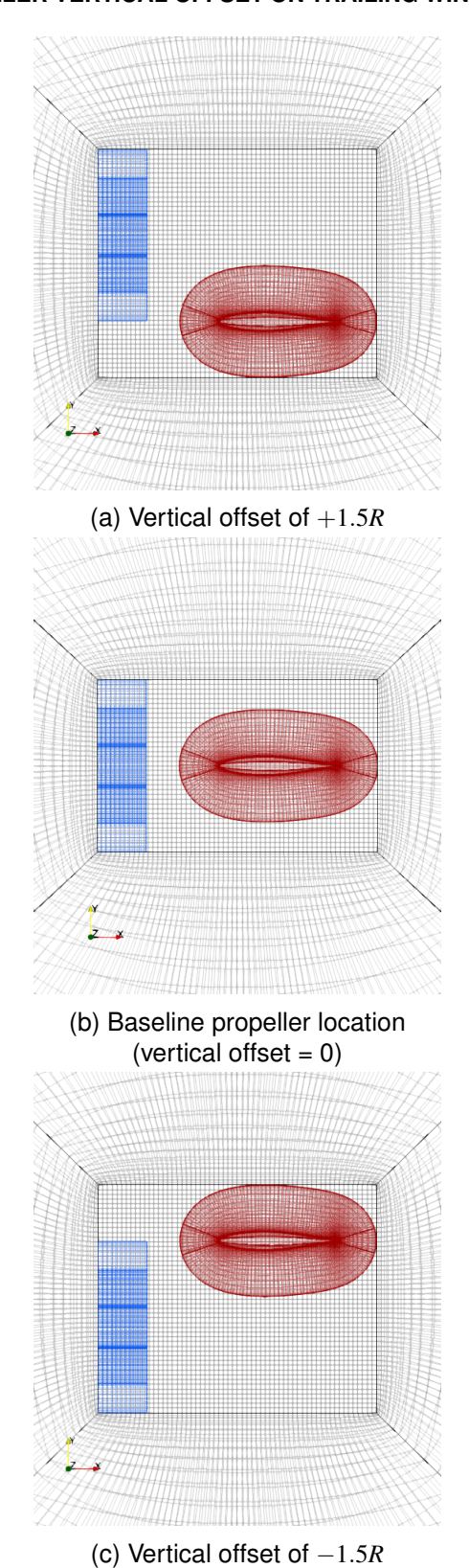


Figure 3 – Side views of the overset meshes for the baseline and extreme propeller locations

# 3.3 Propeller Model Inputs

For the experimental configuration's propeller,  $P/D_{\varnothing}$  ranges from 0.9 at r/R=0.45 to 1.1 at r/R=0.95 [52]. For the propeller model, we use  $P/D_{\varnothing}=1.05$ , which corresponds to the 0.75R location. The tangential-loading model (Eq. (3)) is based on the assumptions that the propeller has a radially constant pitch and that the forces on the blade are locally perpendicular to the blade chords, which

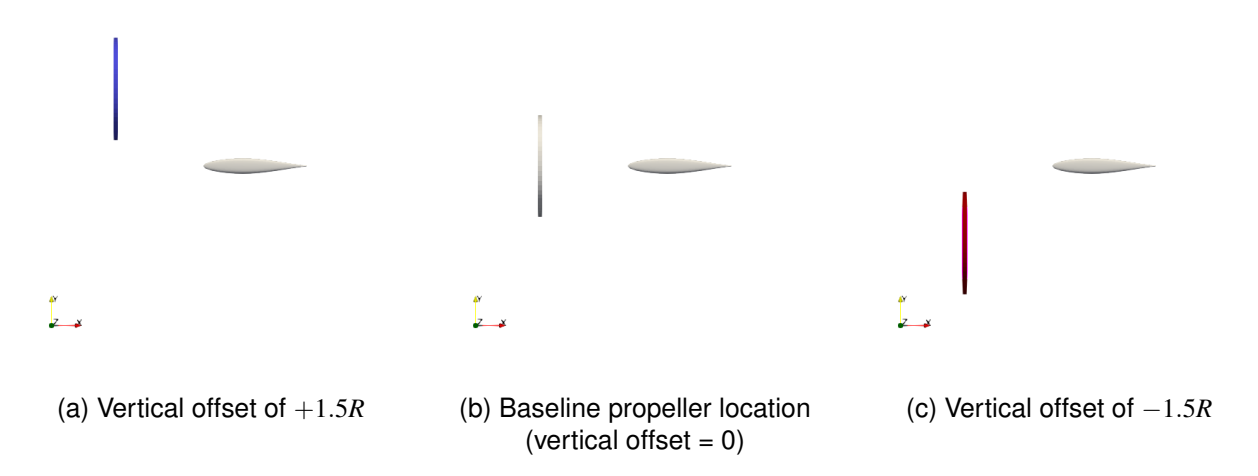


Figure 4 – Side views of the wing and disk surfaces for the baseline and extreme propeller locations

are approximations.

CFD simulations by Stokkermans [35] for this propeller show that the blade root (r = 0.35R to r = 0.15R) generates negative thrust due to thick profiles and flow separation. Therefore, we use  $r_{\rm in} = 0.35R$  in the axial-loading model (Eq. (1)), which results in negative values between r = 0.35R and r = 0.15R. Additionally, for this root portion, we multiply the axial forces from Eq. (1) by 0.25, as the results of Stokkermans [35] show a reduction in slope after the axial force becomes zero at approximately r = 0.35R. This root portion also roughly coincides with the cross-section of the nacelle (r = 0.3R). For the spinner portion (r < 0.15R), we set the axial forces to zero. For the adjustable parameter n, we use n = 0.2, which gives a thrust distribution with the peak near the tip.

For the tangential force distribution, we use Eq. (3) between r=R and r=0.35R and set the forces to zero for r<0.35R. The parameter F is set to a calculated value that makes the total axial force applied to the region outside  $r_{\rm in}$  equal to the specified thrust. We use the region outside  $r_{\rm in}$  for this calculation because Veldhuis [20] noted that the thrust coefficients were computed using a book-keeping approach and pressure measurements. We consider these thrust coefficients to most likely represent the thrust generated by the propeller portion outside the nacelle radius of r=0.3R.

## 4. Results

## 4.1 Angle of Attack = 0 deg

Figures 5 and 6 show the wing sectional lift coefficient ( $C_l$ ) and sectional drag coefficient ( $C_d$ ) distributions, respectively, for the 0 deg AoA cases with inboard-up propeller rotation. Figures 7 and 8 show the same for outboard-up propeller rotation. For this wing, the shapes of the  $C_l$  and  $C_d$  distributions are also the shapes of the wing's lift and drag distributions, respectively, because the chord lengths are constant across the span. Figures 5 and 6 also include experimental results from Veldhuis [20] (zero vertical offset), and they match well with the corresponding CFD results.

When the propeller is moved up or down 0.5R relative to the baseline configuration, there is a similar change in the  $C_l$  distributions. In both cases, there is still a peak and a trough due to the swirl, but of lesser amplitude than when there is no offset. However, the  $C_l$  values are greater across the span for +0.5R than for -0.5R. On the other hand, the corresponding  $C_d$  distributions are more obviously dissimilar and have more striking changes relative to the baseline configuration. What we observe here can be attributed to the combination of three primary factors. The first factor (Factor 1) is a combination of the varying magnitude of the upwash and downwash components of the propeller swirl velocities and the varying extent of the wing inside the propeller's streamtube with respect to vertical offset. The second factor (Factor 2) is the pressure and velocity distributions associated with streamtube contraction, which create upwash (for positive vertical offset) or downwash (for negative vertical

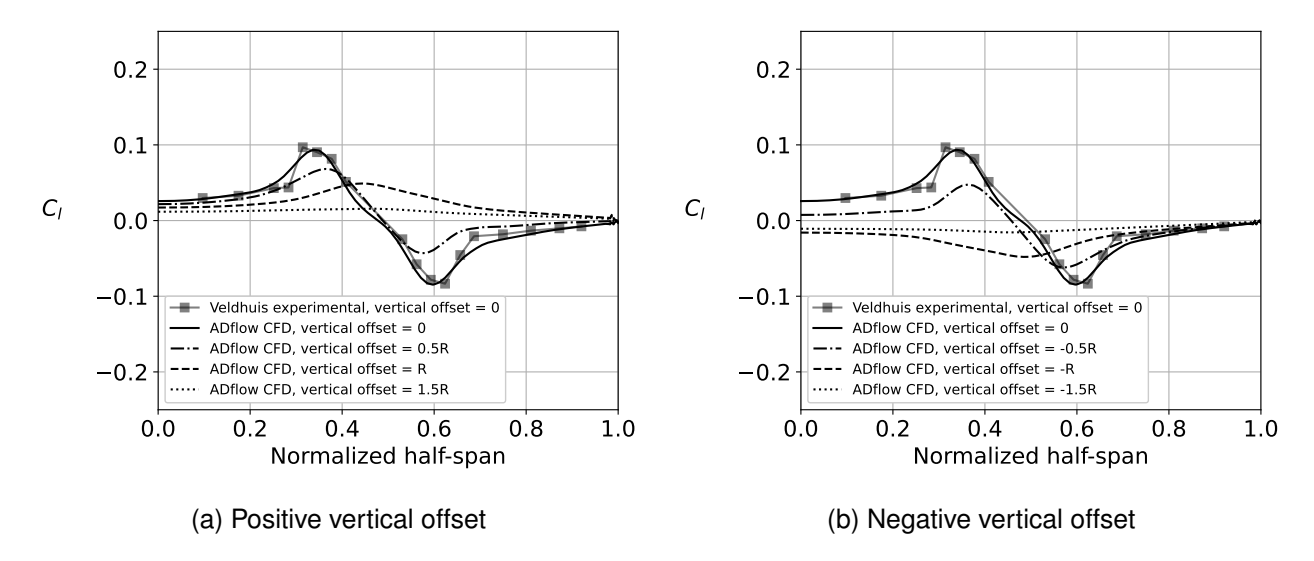


Figure 5 – Wing  $C_l$  distributions for 0 deg AoA with inboard-up propeller rotation (with experimental results from Veldhuis [20])

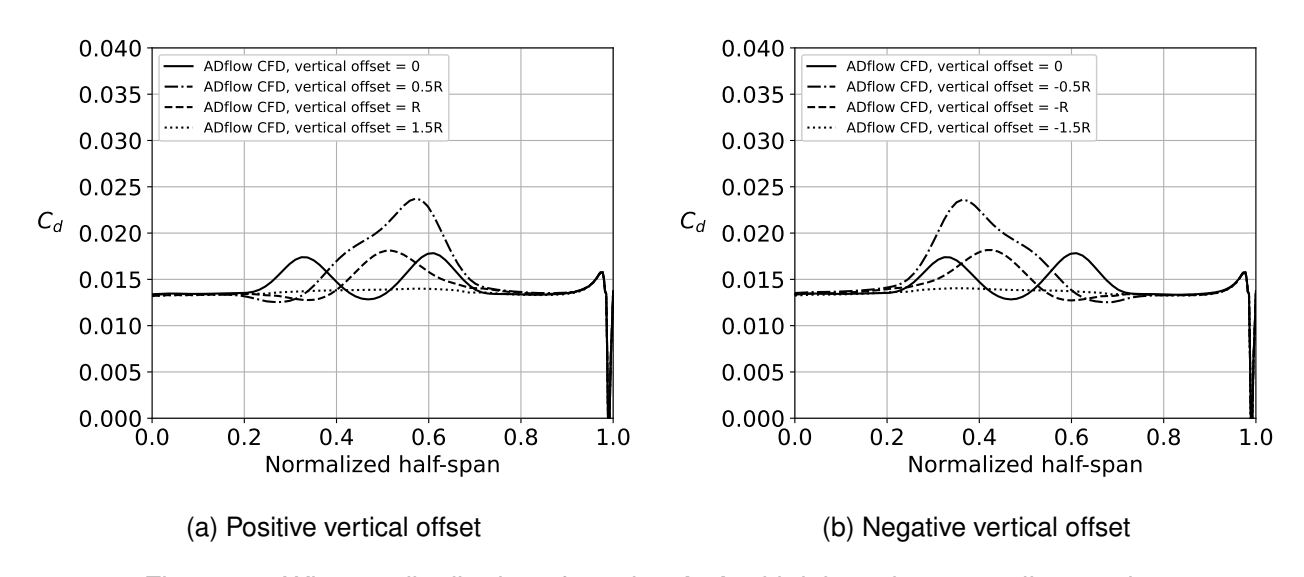


Figure 6 – Wing  $C_d$  distributions for 0 deg AoA with inboard-up propeller rotation

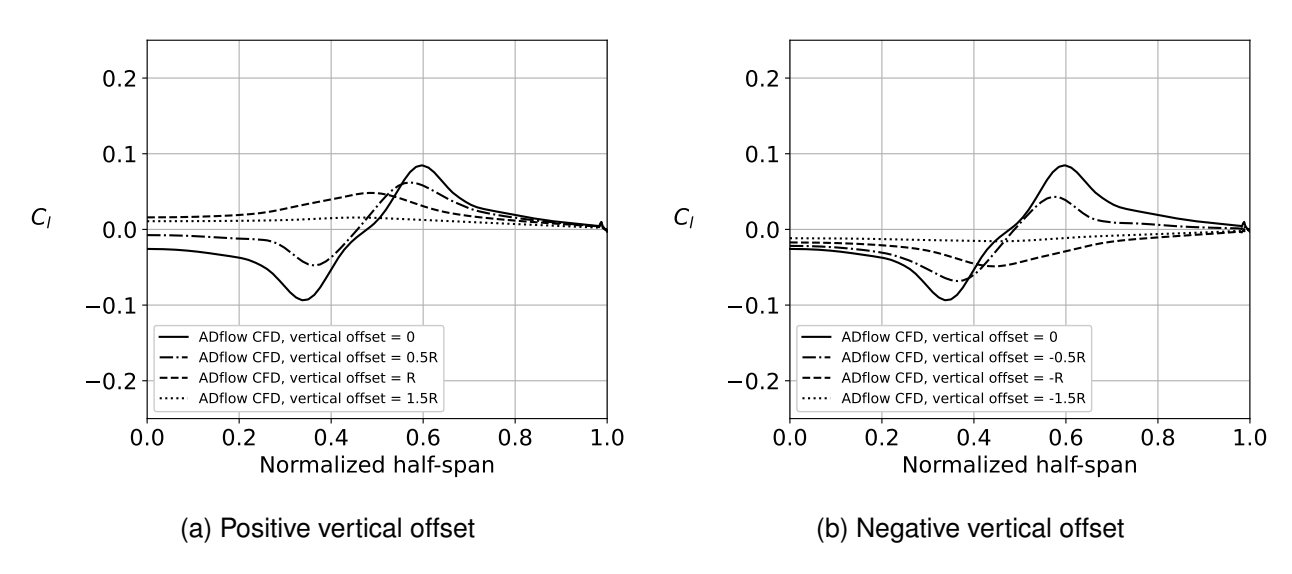


Figure 7 – Wing  $C_l$  distributions for 0 deg AoA with outboard-up propeller rotation

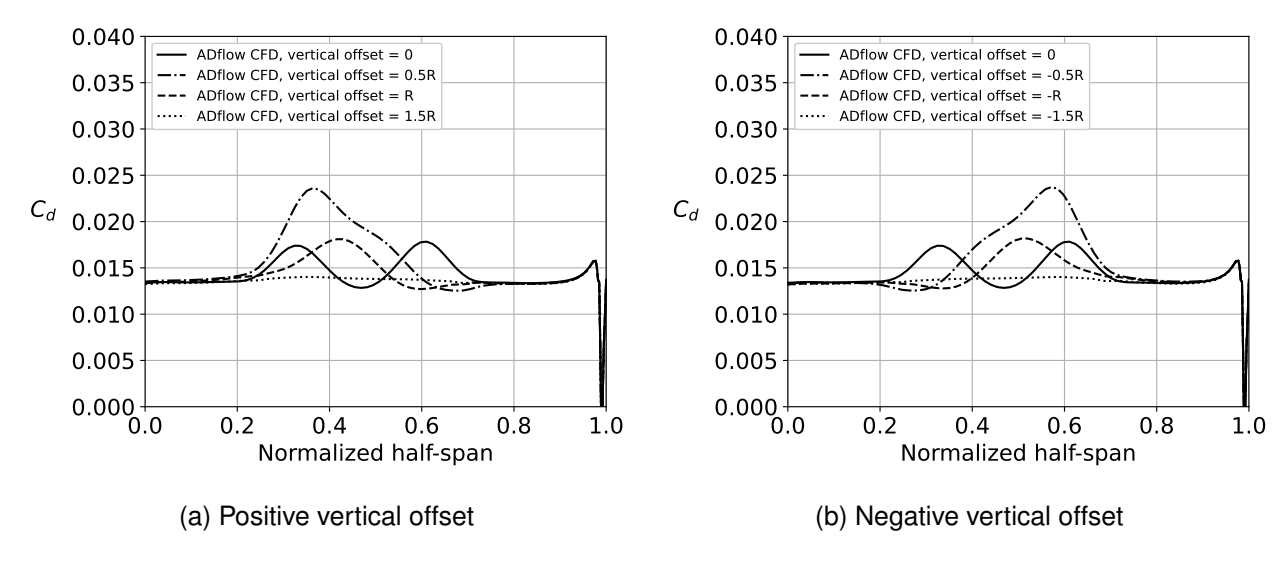


Figure 8 – Wing  $C_d$  distributions for 0 deg AoA with outboard-up propeller rotation

offset) effects. The third factor (Factor 3) is a combination of the non-uniform radial distribution of dynamic pressure in a propeller's streamtube and the varying extent of the wing inside the propeller's streamtube with respect to vertical offset.

When the propeller is moved up or down 1.0R relative to the baseline configuration, we no longer obtain both a peak and a trough in the  $C_l$  distributions but only a peak or a trough of lesser amplitude. There is only a peak for +1.0R and only a trough for -1.0R. Therefore, Factor 2 dominates here. For +1.0R, the peak is slightly more inboard for inboard-up rotation than for outboard-up rotation. For -1.0R, the trough is slightly more inboard for outboard-up rotation than for inboard-up rotation. The corresponding  $C_d$  distributions for both inboard-up and outboard-up rotations have a primary peak of similar amplitude to the baseline cases but only a slight trough. The trough is inboard for +1.0R with inboard-up rotation and for -1.0R with outboard-up rotation. This asymmetry and the greater amplitude of the peak than the trough for both propeller rotation directions and both positive and negative offsets show that there is still an interplay here between Factors 1, 2, and 3.

When the propeller is moved up or down 1.5R relative to the baseline configuration, the propeller effects almost vanish. The  $C_l$  across the span is slightly above zero for +1.5R and slightly below zero for -1.5R.

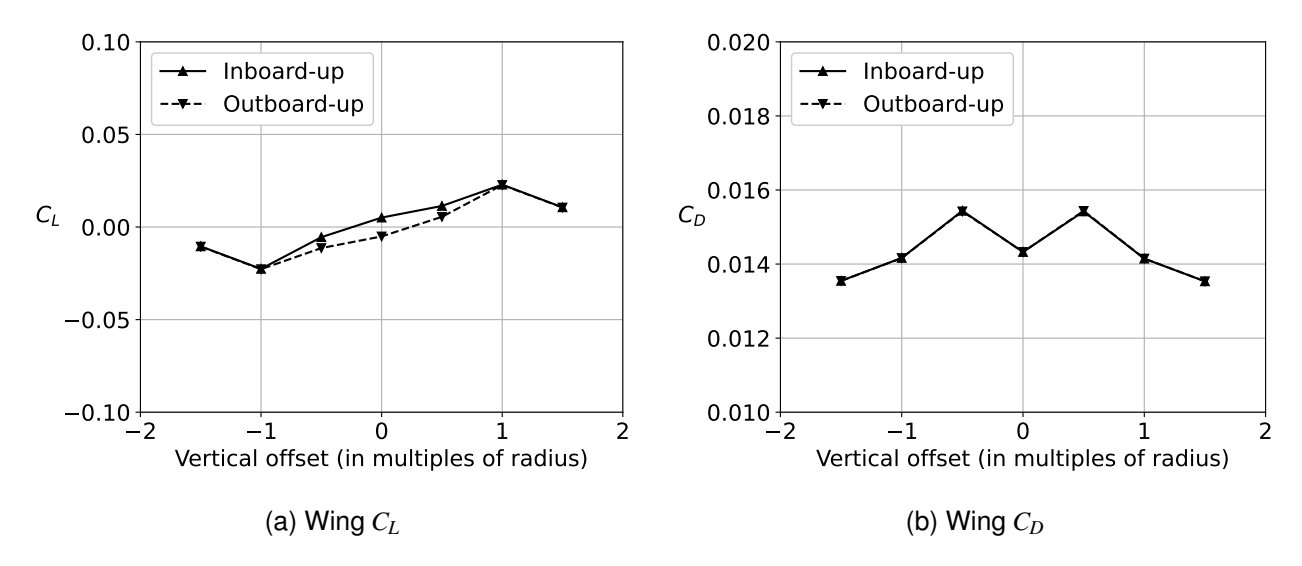


Figure 9 – ADflow CFD results for wing  $C_L$  and  $C_D$  at 0 deg AoA for both inboard-up and outboard-up propeller rotation

Figures 9a and 9b show the integrated lift coefficients ( $C_L$ ) and drag coefficients ( $C_D$ ) of the wing as a function of the vertical offset for both inboard-up and outboard-up propeller rotation for the 0 deg AoA cases. These show non-monotonic anti-symmetric (for  $C_L$ ) and symmetric (for  $C_D$ ) trends with respect to vertical offset, consistent with the results presented by Veldhuis [20].

Figures 15 to 18 in the Appendix show the pressure coefficient  $(C_p)$  distributions at three wing sections for the 0 deg AoA cases. These provide a more detailed picture of how Factors 1 and 2 affect the pressure distributions.

# 4.2 Angle of Attack = 4 deg

Figures 10 and 11 show the wing  $C_l$  and  $C_d$  distributions, respectively, for the 4 deg AoA cases with inboard-up propeller rotation. Figures 12 and 13 show the same for outboard-up propeller rotation. Figures 10 and 11 also include experimental results from Veldhuis [20] (zero vertical offset), and they match reasonably well with the corresponding CFD results.

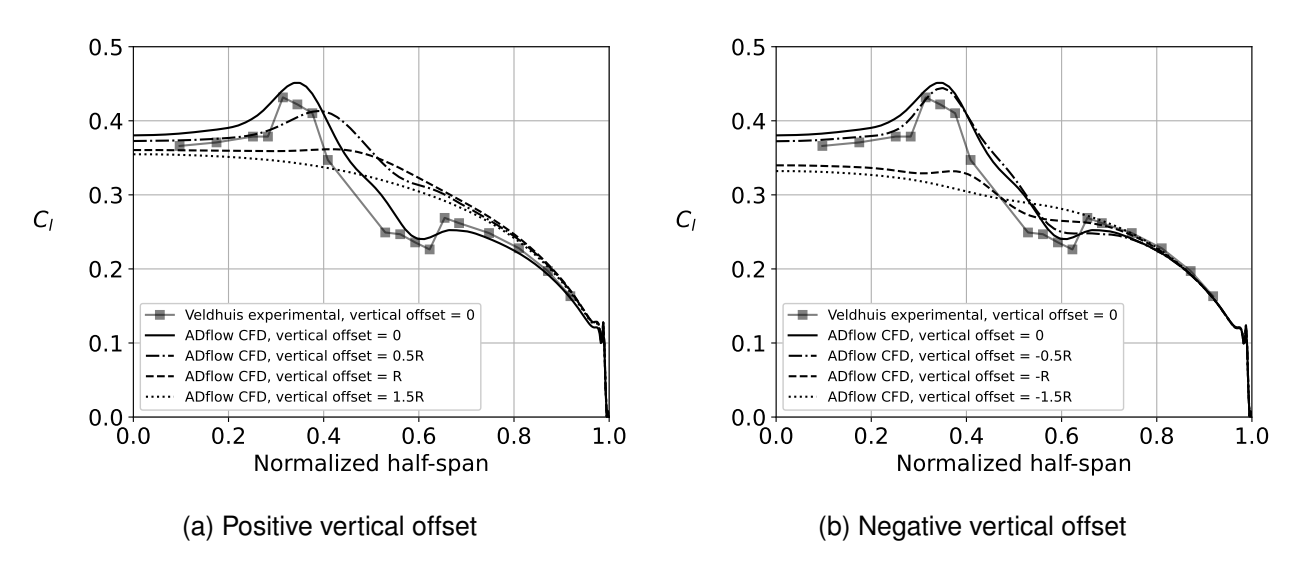


Figure 10 – Wing  $C_l$  distributions for 4 deg AoA with inboard-up propeller rotation (with experimental results from Veldhuis [20])

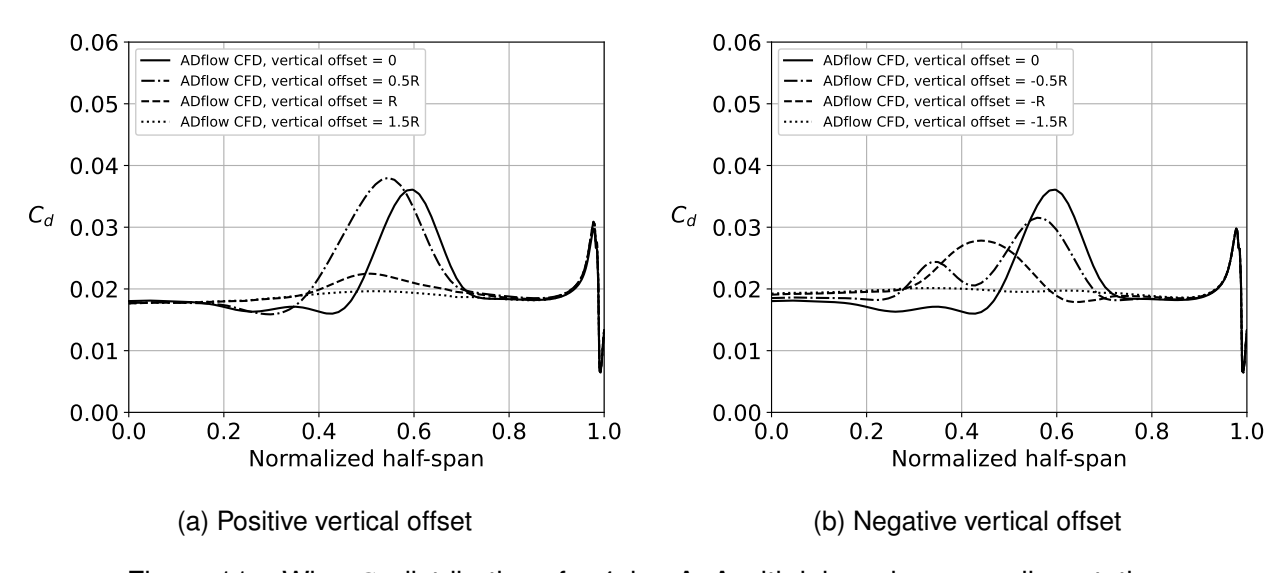


Figure 11 – Wing  $C_d$  distributions for 4 deg AoA with inboard-up propeller rotation

When the propeller is moved up or down 0.5R relative to the baseline configuration, there are more noticeably different changes in the  $C_l$  distributions here than for the 0 deg cases. For -0.5R, the  $C_l$  distribution is almost unchanged. However, for +0.5R, there is only a peak that is wider and of

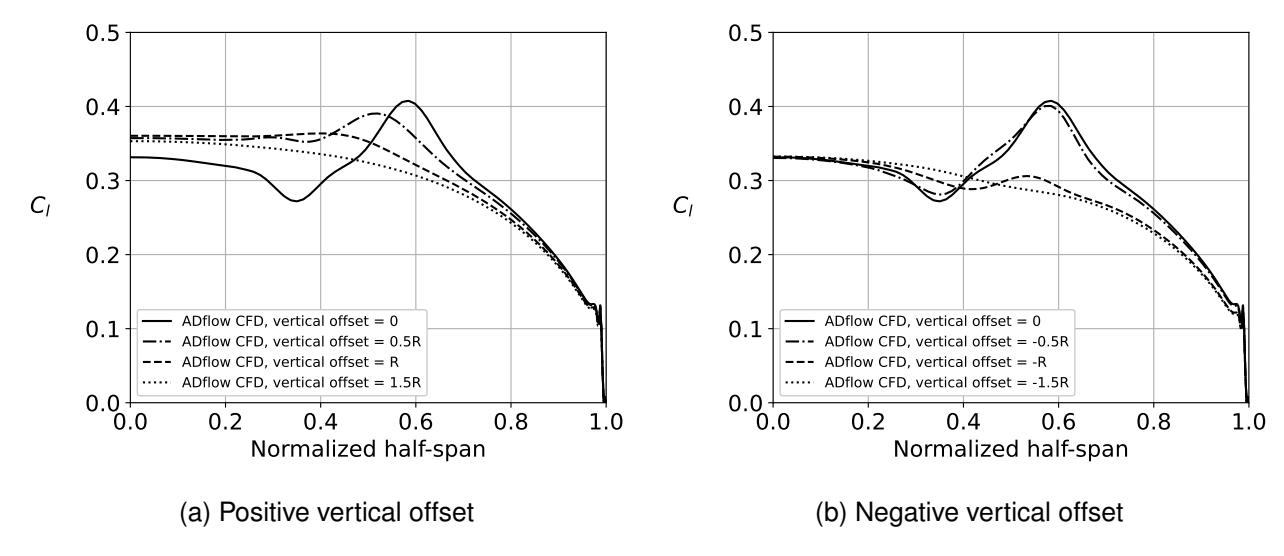


Figure 12 – Wing  $C_l$  distributions for 4 deg AoA with outboard-up propeller rotation

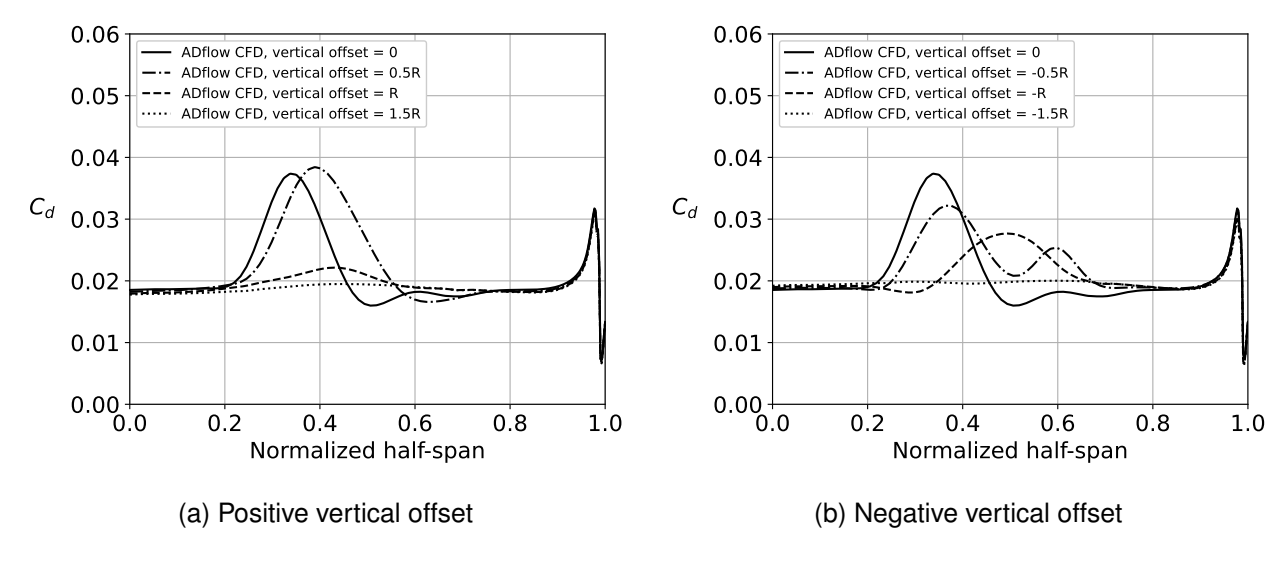


Figure 13 – Wing  $C_d$  distributions for 4 deg AoA with outboard-up propeller rotation

lesser amplitude. The corresponding  $C_d$  distributions are also clearly dissimilar. For +0.5R, there is one peak, and for -0.5R, there are two peaks. What we observe here can be attributed to the combination of Factors 1, 2, and 3.

When the propeller is moved up or down 1.0R relative to the baseline configuration, the propeller effects in the  $C_l$  distributions are significantly diminished but still visible. There is only a peak of small amplitude for +1.0R and a slight peak and a slight trough for -1.0R. The corresponding  $C_d$  distributions all have a peak, with the peaks for -1.0R having significantly greater amplitude. Here, we again observe the interplay of Factors 1, 2, and 3.

When the propeller is moved up or down 1.5R relative to the baseline configuration, the propeller effects almost vanish. The  $C_d$  values for the inboard half of the wing are slightly lower for 1.5R than for -1.5R.

Figures 14a and 14b show the  $C_L$  and  $C_D$  of the wing as a function of the vertical offset for both inboard-up and outboard-up propeller rotation for the 4 deg AoA cases. Both the  $C_L$  and the  $C_D$  are highest for 0.5R. The corresponding lift-to-drag ratios (L/D) plotted in Fig. 14c show that the lowest and highest L/D are obtained when the vertical offset is -1.0R and 1.0R, respectively. These non-monotonic and asymmetric trends with respect to vertical offset are consistent with the results presented by Veldhuis [20].

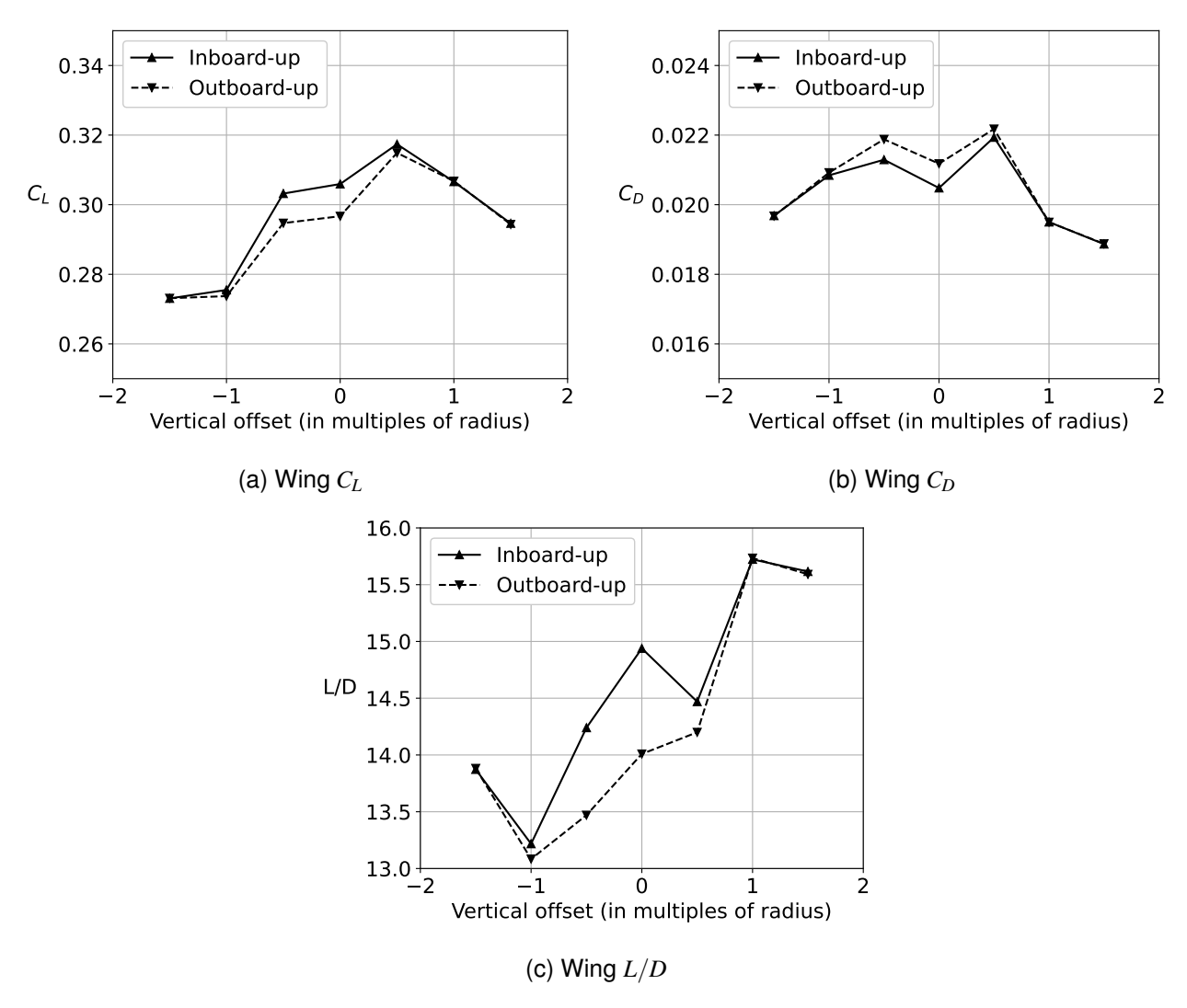


Figure 14 – ADflow CFD results for wing  $C_L$ ,  $C_D$ , and L/D at 4 deg AoA for both inboard-up and outboard-up propeller rotation

Figures 19 to 22 in the Appendix show the  $C_p$  distributions at three wing sections for the 4 deg AoA cases. These provide a more detailed picture of how Factors 1 and 2 affect the pressure distributions.

## 5. Conclusions

In this paper, we present simulation results for a rectangular wing with an inboard tractor propeller using steady RANS CFD and an actuator-disk approach. These results are for 0 and 4 deg AoA and propeller-wing vertical offsets ranging from -1.5R to +1.5R, for both inboard-up and outboard-up propeller rotation.

The results show that changing the propeller-wing vertical offset can significantly change a trailing wing's lift and drag distributions, and these distributions have a strong dependence on the direction of the vertical offset. The results also show an interplay of three primary factors:

- 1. Factor 1 is a combination of the varying magnitude of the upwash and downwash components of the propeller swirl velocities and the varying extent of the wing inside the propeller's streamtube with respect to vertical offset.
- 2. Factor 2 is the pressure and velocity distributions associated with streamtube contraction, which create upwash (for positive vertical offset) or downwash (for negative vertical offset) effects.

3. Factor 3 is a combination of the non-uniform radial distribution of dynamic pressure in a propeller's streamtube and the varying extent of the wing inside the propeller's streamtube with respect to vertical offset.

The interplay of these factors results in trends that are non-monotonic and asymmetric with respect to propeller-wing vertical offset.

# 6. Acknowledgments

The authors acknowledge the support provided by Fundação de Amparo à Pesquisa do Estado de São Paulo, FAPESP, under Research Grant No. 2013/07375-0, and by Conselho Nacional de Desenvolvimento Científico e Tecnológico, CNPq, under Research Grant No. 315411/2023-6.

## 7. Contact Author Email Address

Shamsheer S. Chauhan: sschau@umich.edu

Gustavo Padovany da Silva: guspadovany@gmail.com Gustavo L. O. Halila: gustavo.halila@embraer.com.br

Joaquim R. R. A. Martins: jrram@umich.edu

João Luiz F. Azevedo: joaoluiz.azevedo@gmail.com

# 8. Copyright Statement

The authors confirm that they, and/or their company or organization, hold copyright on all of the original material included in this paper. The authors also confirm that they have obtained permission, from the copyright holder of any third party material included in this paper, to publish it as part of their paper. The authors confirm that they give permission, or have obtained permission from the copyright holder of this paper, for the publication and distribution of this paper as part of the ICAS proceedings or as individual off-prints from the proceedings.

## References

- [1] Prandtl, L., "Mutual Influence of Wings and Propeller," Technical Note NACA-TN-74, NACA, December 1921, An English translation of an extract from the First Report of the Göttingen Aerodynamic Laboratory, Chapter 4, Section 6, pp. 112–118.
- [2] Kuhn, R. E. and Draper, J. W., "An investigation of a wing-propeller configuration employing large-chord plain flaps and large-diameter propellers for low-speed flight and vertical take-off," Technical Note NACA-TN-3307, NACA, January 1954.
- [3] Kuhn, R. E. and Draper, J. W., "Investigation of the Aerodynamic Characteristics of a Model Wing-Propeller Combination and of the Wing and Propeller Separately at Angles of Attack up to 90°," Technical Report NACA-TR-1263, NASA, January 1956.
- [4] McCormick, B. W., Aerodynamics of V/STOL Flight, Academic Press, 1st ed., 1967.
- [5] Moore, M. D. and Fredericks, B., "Misconceptions of Electric Aircraft and their Emerging Aviation Markets," AIAA Paper No. 2014-0535, 52nd Aerospace Sciences Meeting, AIAA, January 2014.
- [6] Stoll, A. M., Bevirt, J., Pei, P. P., and Stilson, E. V., "Conceptual Design of the Joby S2 Electric VTOL PAV," AIAA Paper No. 2014-2407, 14th AIAA Aviation Technology, Integration, and Operations Conference, AIAA, June 2014.
- [7] Deere, K. A., Viken, S. A., Carter, M. B., Viken, J. K., Derlaga, J. M., and Stoll, A. M., "Comparison of High-Fidelity Computational Tools for Wing Design of a Distributed Electric Propulsion Aircraft," AIAA Paper No. 2017-3925, 35th AIAA Applied Aerodynamics Conference, AIAA, June 2017.
- [8] Droandi, G., Syal, M., and Bower, G., "Tiltwing Multi-Rotor Aerodynamic Modeling in Hover, Transition and Cruise Flight Conditions," AHS Paper No. 74-2018-1267, AHS International Forum 74, May 2018.
- [9] de Vries, R., Brown, M., and Vos, R., "Preliminary Sizing Method for Hybrid-Electric Distributed-Propulsion Aircraft," *Journal of Aircraft*, Vol. 56, No. 6, 2019, pp. 2172–2188.

- [10] Chauhan, S. S. and Martins, J. R. A., "Tilt-wing eVTOL takeoff trajectory optimization," *Journal of Aircraft*, Vol. 57, No. 1, January 2020, pp. 93–112.
- [11] Chauhan, S. S. and Martins, J. R. A., "RANS-Based Aerodynamic Shape Optimization of a Wing Considering Propeller-Wing Interaction," *Journal of Aircraft*, Vol. 58, No. 3, May 2021, pp. 497–513.
- [12] Courtin, C., Mahseredjian, A., Dewald, A. J., Drela, M., and Hansman, J., "A Performance Comparison of eSTOL and eVTOL Aircraft," *AIAA AVIATION 2021 FORUM*, 2021.
- [13] Koyuncuoglu, H. U. and He, P., "Simultaneous wing shape and actuator parameter optimization using the adjoint method," *Aerospace Science and Technology*, Vol. 130, 2022.
- [14] Pacini, B., Prajapati, M., Duraisamy, K., Martins, J. R. R. A., and He, P., "Understanding Distributed Propulsion on the NASA Tiltwing Concept Vehicle with Aerodynamic Shape Optimization," AIAA Paper No. 2023-0143, *AIAA Scitech Forum 2023*, January 2023.
- [15] Alvarez, E. J. and Ning, A., "Meshless Large-Eddy Simulation of Propeller–Wing Interactions with Reformulated Vortex Particle Method," *Journal of Aircraft*, 2024.
- [16] Chauhan, S. S. and Martins, J. R. A., "RANS-Based Aerodynamic Shape Optimization of a Wing with a Propeller in Front of the Wingtip," *Aerospace*, Vol. 11, No. 7, 2024.
- [17] Snyder, Jr., M. H. and Zumwalt, G. W., "Effects of wingtip-mounted propellers on wing lift and induced drag," *Journal of Aircraft*, Vol. 6, No. 5, 1969, pp. 392–397.
- [18] Kroo, I., "Propeller-wing integration for minimum induced loss," *Journal of Aircraft*, Vol. 23, No. 7, 1986, pp. 561–565.
- [19] Miranda, L. R. and Brennan, J. E., "Aerodynamic effects of wingtip-mounted propellers and turbines," AIAA Paper No. 1986-1802, 4th Applied Aerodynamics Conference, AIAA, June 1986.
- [20] Veldhuis, L. L. M., *Propeller Wing Aerodynamic Interference*, Ph.D. thesis, Delft University of Technology, 2005.
- [21] Sinnige, T., van Arnhem, N., Stokkermans, T. C. A., Eitelberg, G., and Veldhuis, L. L. M., "Wingtip-Mounted Propellers: Aerodynamic Analysis of Interaction Effects and Comparison with Conventional Layout," *Journal of Aircraft*, Vol. 56, No. 1, 2019, pp. 295–312.
- [22] Whitfield, D. L. and Jameson, A., "Euler equation simulation of propeller-wing interaction in transonic flow," *Journal of Aircraft*, Vol. 21, No. 11, 1984, pp. 835–839.
- [23] Witkowski, D. P., Lee, A. K. H., and Sullivan, J. P., "Aerodynamic interaction between propellers and wings," *Journal of Aircraft*, Vol. 26, No. 9, 1989, pp. 829–836.
- [24] Ardito Marretta, R. M., Davi, G., Milazzo, A., and Lombardi, G., "Wing Pitching and Loading with Propeller Interference," *Journal of Aircraft*, Vol. 36, No. 2, 1999, pp. 468–471.
- [25] Veldhuis, L. L. M. and Heyma, P. M., "Aerodynamic optimisation of wings in multi-engined tractor propeller arrangements," *Aircraft Design*, Vol. 3, No. 3, September 2000, pp. 129–149.
- [26] Moens, F. and Gardarein, P., "Numerical simulation of the propeller/wing interactions for transport aircraft," AIAA Paper No. 2001-2404, 19th AIAA Applied Aerodynamics Conference, June 2001.
- [27] Roosenboom, E. W. M., Stürmer, A., and Schröder, A., "Advanced Experimental and Numerical Validation and Analysis of Propeller Slipstream Flows," *Journal of Aircraft*, Vol. 47, No. 1, 2010, pp. 284–291.
- [28] Stoll, A. M., Bevirt, J., Moore, M. D., Fredericks, W. J., and Borer, N. K., "Drag Reduction Through Distributed Electric Propulsion," AIAA Paper No. 2014-2851, 14th AIAA Aviation Technology, Integration, and Operations Conference, AIAA, June 2014.
- [29] Gomariz-Sancha, A., Maina, M., and Peace, A. J., "Analysis of propeller-airframe interaction effects through a combined numerical simulation and wind-tunnel testing approach," AIAA Paper No. 2015-1026, 53rd AIAA Aerospace Sciences Meeting, AIAA, January 2015.
- [30] Rakshith, B. R., Deshpande, S. M., Narasimha, R., and Praveen, C., "Optimal Low-Drag Wing Planforms for Tractor-Configuration Propeller-Driven Aircraft," *Journal of Aircraft*, Vol. 52, No. 6, 2015, pp. 1791– 1801.
- [31] Hwang, J. T. and Ning, A., "Large-scale multidisciplinary optimization of an electric aircraft for on-demand mobility," AIAA Paper No. 2018-1384, 2018 AIAA/ASCE/AHS/ASC Structures, Structural Dynamics, and Materials Conference, Kissimmee, FL, January 2018.
- [32] Alba, C., Elham, A., German, B. J., and Veldhuis, L. L. M., "A surrogate-based multi-disciplinary design optimization framework modeling wing-propeller interaction," *Aerospace Science and Technology*, Vol. 78, July 2018, pp. 721–733.
- [33] Epema, K., Wing Optimisation for Tractor Propeller Configurations, Master's thesis, Delft University of Technology, 2017.
- [34] Moore, K. R. and Ning, A., "Takeoff and Performance Trade-Offs of Retrofit Distributed Electric Propulsion for Urban Transport," *Journal of Aircraft*, Vol. 56, No. 5, 2019, pp. 1880–1892.

- [35] Stokkermans, T. C. A., van Arnhem, N., Sinnige, T., and Veldhuis, L. L. M., "Validation and Comparison of RANS Propeller Modeling Methods for Tip-Mounted Applications," *AIAA Journal*, Vol. 57, No. 2, 2019, pp. 566–580.
- [36] Stokkermans, T., Veldhuis, L., Soemarwoto, B., Fukari, R., and Eglin, P., "Breakdown of aerodynamic interactions for the lateral rotors on a compound helicopter," *Aerospace Science and Technology*, Vol. 101, 2020.
- [37] van Arnhem, N., de Vries, R., Sinnige, T., Vos, R., and Veldhuis, L. L. M., "Aerodynamic Performance and Static Stability Characteristics of Aircraft with Tail-Mounted Propellers," *Journal of Aircraft*, Vol. 59, No. 2, 2022, pp. 415–432.
- [38] Russo, O., Aprovitola, A., de Rosa, D., Pezzella, G., and Viviani, A., "Computational Fluid Dynamics Analyses of a Wing with Distributed Electric Propulsion," *Aerospace*, Vol. 10, No. 1, 2023.
- [39] Pedreiro, L. N., Estudo e otimização de uma asa sob efeito de hélice na configuração tractor para redução de arrasto, Master's thesis, Universidade Federal de Minas Gerais, 2017.
- [40] Martins, J. R. A., "Aerodynamic Design Optimization: Challenges and Perspectives," *Computers & Fluids*, Vol. 239, 2022, pp. 105391.
- [41] Yildirim, A., Kenway, G. K. W., Mader, C. A., and Martins, J. R. R. A., "A Jacobian-free approximate Newton–Krylov startup strategy for RANS simulations," *Journal of Computational Physics*, Vol. 397, November 2019, pp. 108741.
- [42] Mader, C. A., Kenway, G. K. W., Yildirim, A., and Martins, J. R. A., "ADflow: An open-source computational fluid dynamics solver for aerodynamic and multidisciplinary optimization," *Journal of Aerospace Information Systems*, Vol. 17, No. 9, September 2020, pp. 508–527.
- [43] Lee, Y. and Baeder, J., "Implicit hole cutting—a new approach to overset grid connectivity," AIAA Paper No. 2003-4128, 16th AIAA Computational Fluid Dynamics Conference, 2003.
- [44] Landmann, B. and Montagnac, M., "A highly automated parallel Chimera method for overset grids based on the implicit hole cutting technique," *International Journal for Numerical Methods in Fluids*, Vol. 66, No. 6, 2011, pp. 778–804.
- [45] Kenway, G. K. W., Secco, N., Martins, J. R. R. A., Mishra, A., and Duraisamy, K., "An Efficient Parallel Overset Method for Aerodynamic Shape Optimization," AIAA Paper No. 2017-0357, *Proceedings of the 58th AIAA/ASCE/AHS/ASC Structures, Structural Dynamics, and Materials Conference, AIAA SciTech Forum*, Grapevine, TX, January 2017.
- [46] Spalart, P. and Allmaras, S., "A One-Equation Turbulence Model for Aerodynamic Flows," 30th Aerospace Sciences Meeting and Exhibit, June 1992.
- [47] Jameson, A. J., Schmidt, W., and Turkel, E., "Numerical Solution of the Euler Equations by a Finite-Volume Method Using Runge-Kutta Time-Stepping Schemes," AIAA Paper No. 1981-1259, 14th AIAA Fluid and Plasma Dynamics Conference, Palo Alto, CA, June 1981.
- [48] Secco, N., Kenway, G. K. W., He, P., Mader, C. A., and Martins, J. R. A., "Efficient Mesh Generation and Deformation for Aerodynamic Shape Optimization," *AIAA Journal*, Vol. 59, No. 4, April 2021, pp. 1151–1168.
- [49] Chan, W. M. and Steger, J. L., "Enhancements of a three-dimensional hyperbolic grid generation scheme," *Applied Mathematics and Computation*, Vol. 51, No. 2–3, 1992, pp. 181–205.
- [50] Hoekstra, M., "A RANS-based analysis tool for ducted propeller systems in open water condition," *International Shipbuilding Progress 53*, Vol. 53, 2006, pp. 205–227.
- [51] Selig, M., "University of Illinois Urbana-Champaign Airfoil Data Site," https://m-selig.ae.illinois.edu/ads/coord\_database.html.
- [52] Sinnige, T., de Vries, R., Corte, B. D., Avallone, F., Ragni, D., Eitelberg, G., and Veldhuis, L. L. M., "Unsteady Pylon Loading Caused by Propeller-Slipstream Impingement for Tip-Mounted Propellers," *Journal of Aircraft*, Vol. 55, No. 4, 2018, pp. 1605–1618.

## **Appendix A: Pressure Coefficient Distributions**

Figures 15 to 18 show the  $C_p$  distributions for three wing sections for the 0 deg AoA cases. Figures 19 to 22 show the  $C_p$  distributions for the same sections for the 4 deg AoA cases. The three wing sections are at an inboard location behind the propeller (35% b/2), the propeller axis location (47% b/2), and an outboard location behind the propeller (62% b/2). The relevant plots also include experimental results from Veldhuis [20] for the baseline configuration at 4 deg AoA with inboard-up propeller rotation.

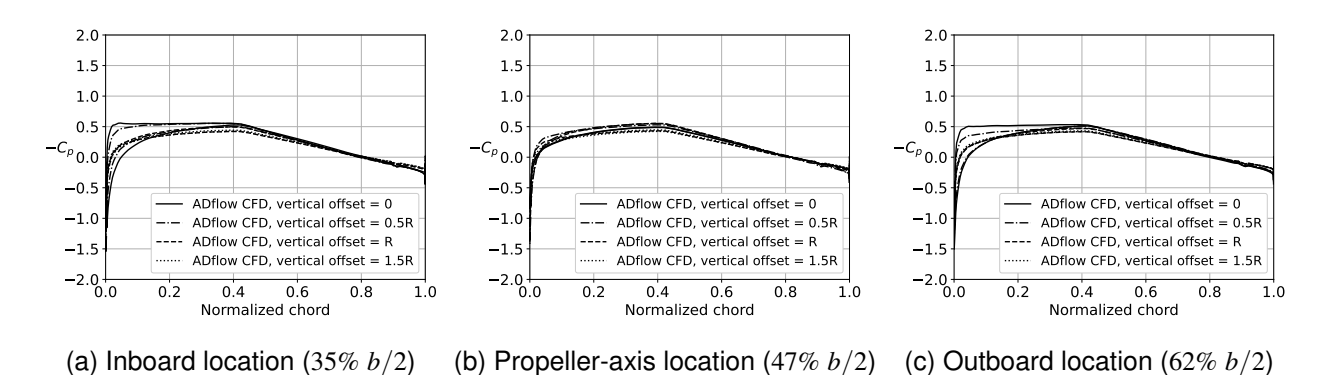


Figure  $15 - C_p$  distributions for the 0 deg AoA cases with inboard-up propeller rotation and positive vertical offsets

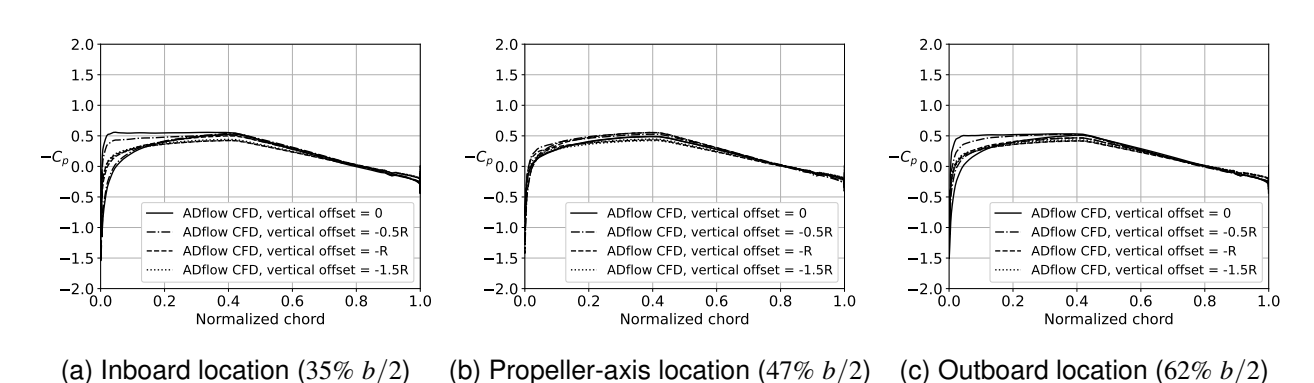


Figure  $16 - C_p$  distributions for the 0 deg AoA cases with inboard-up propeller rotation and negative vertical offsets

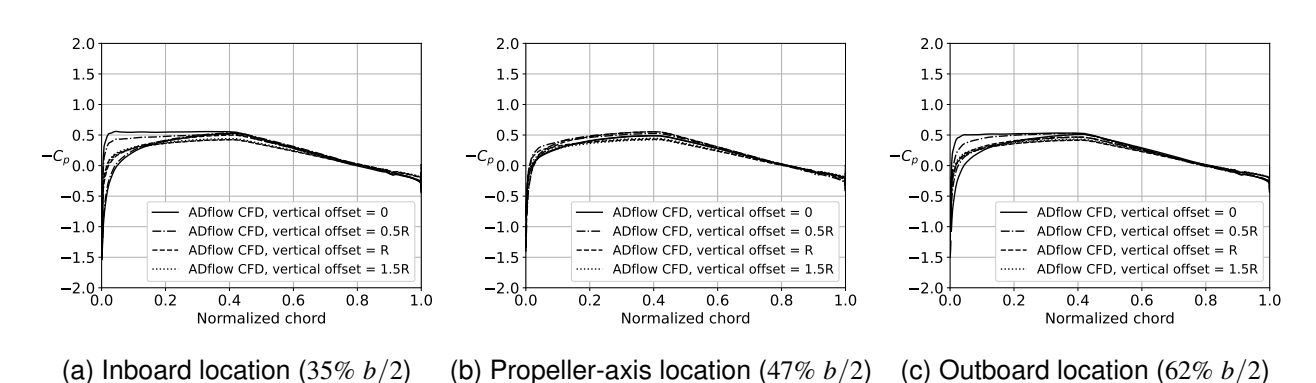
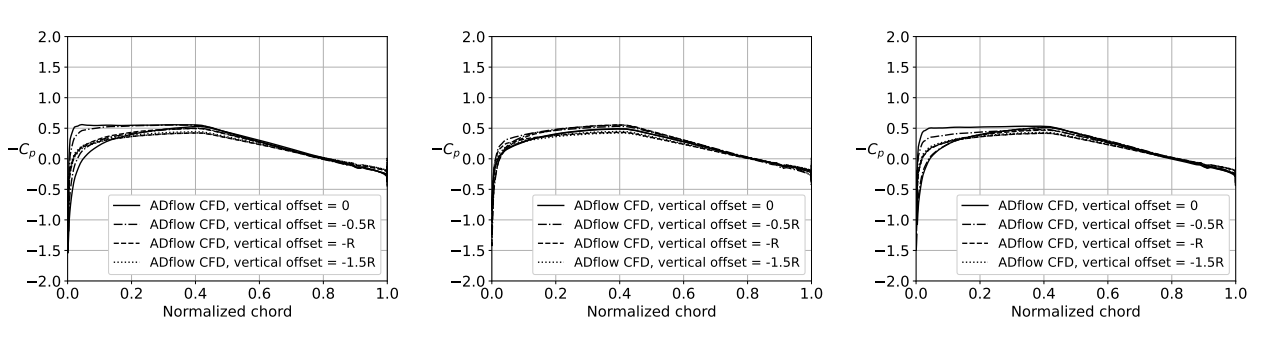


Figure  $17 - C_p$  distributions for the 0 deg AoA cases with outboard-up propeller rotation and positive vertical offsets



(a) Inboard location (35% b/2) (b) Propeller-axis location (47% b/2) (c) Outboard location (62% b/2)

Figure  $18 - C_p$  distributions for the 0 deg AoA cases with outboard-up propeller rotation and negative vertical offsets

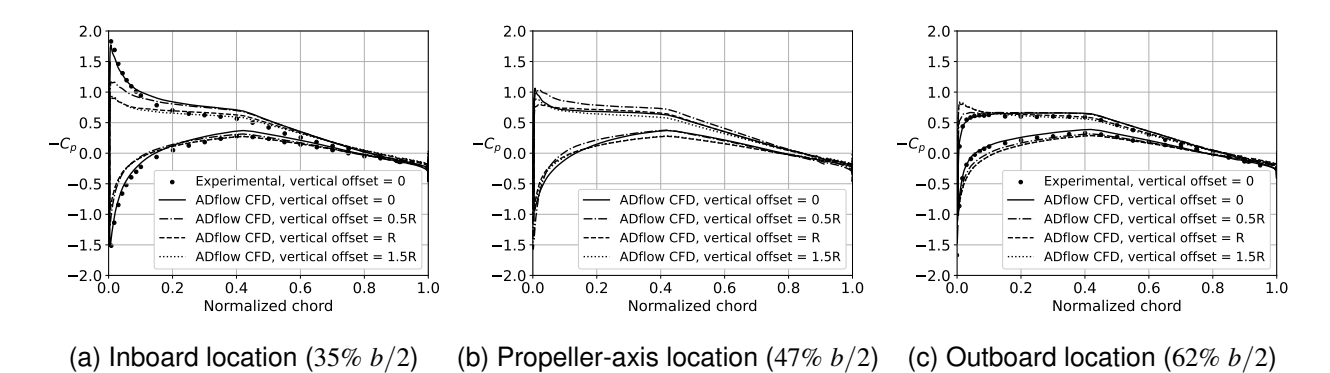


Figure  $19 - C_p$  distributions for the 4 deg AoA cases with inboard-up propeller rotation and positive vertical offsets (with experimental results from Veldhuis [20])

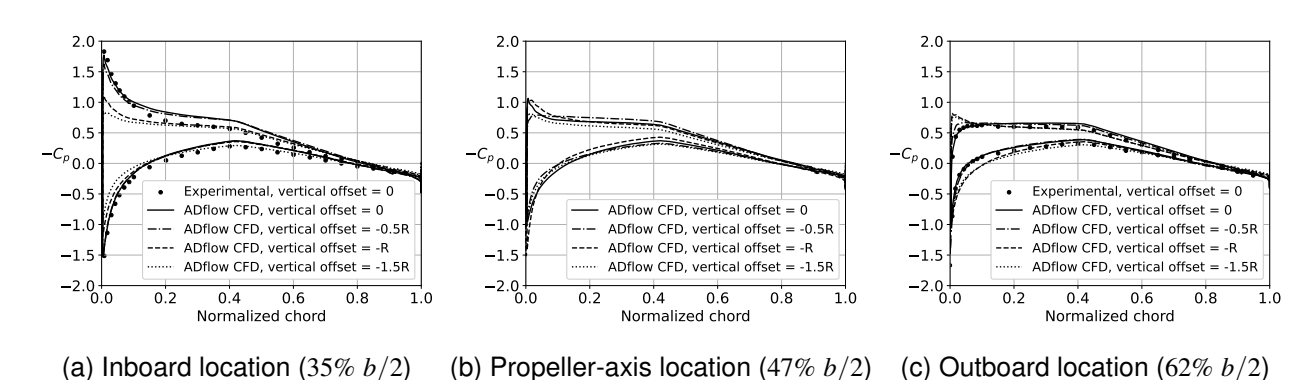


Figure  $20 - C_p$  distributions for the 4 deg AoA cases with inboard-up propeller rotation and negative vertical offsets (with experimental results from Veldhuis [20])

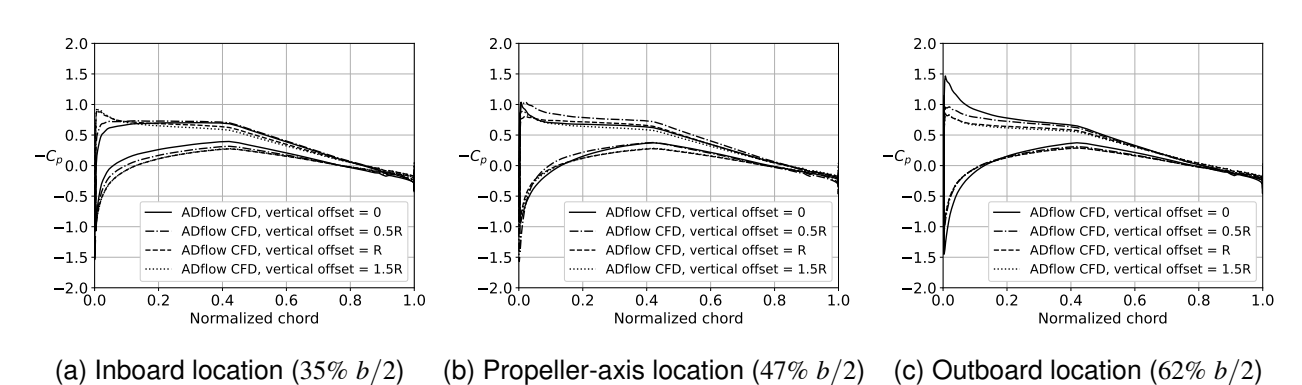
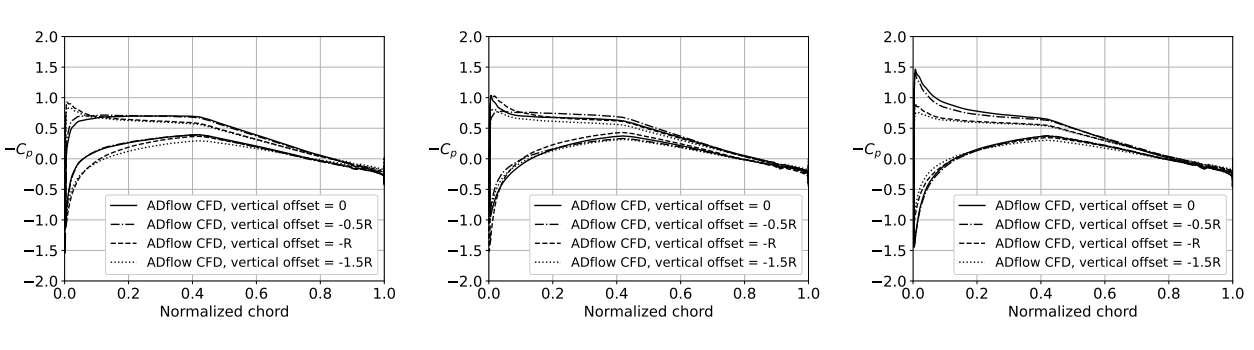


Figure 21 –  $C_p$  distributions for the 4 deg AoA cases with outboard-up propeller rotation and positive vertical offsets



(a) Inboard location (35% b/2) (b) Propeller-axis location (47% b/2) (c) Outboard location (62% b/2)

Figure  $22 - C_p$  distributions for the 4 deg AoA cases with outboard-up propeller rotation and negative vertical offsets